

---

# 3D ScatterNet: Inference from 21 cm Light-cones

---

Xiaosheng Zhao<sup>1,2</sup> Shifan Zuo<sup>3,4</sup> Yi Mao<sup>1</sup>

## Abstract

The Square Kilometre Array (SKA) will have the sensitivity to take the 3D light-cones of the 21 cm signal from the epoch of reionization. This signal, however, is highly non-Gaussian and can not be fully interpreted by the traditional statistic using power spectrum. In this work, we introduce the 3D ScatterNet that combines the normalizing flows with solid harmonic wavelet scattering transform, a 3D CNN featurizer with inductive bias, to perform implicit likelihood inference (ILI) from 21 cm light-cones. We show that 3D ScatterNet outperforms the ILI with a fine-tuned 3D CNN in the literature. It also reaches better performance than ILI with the power spectrum for varied light-cone effects and varied signal contaminations.

## 1. Introduction

The 21 cm fields from the epoch of reionization are highly non-Gaussian resulting from the patch reionization. Maximally exploiting the full information in the 21 cm fields needs new statistics besides the 21 cm power spectrum. Machine learning methods like the convolutional neural networks (CNNs) are promising tools for astrophysical parameter estimation directly from 2D fields or 3D light-cones (Gillet et al., 2019; Prelogović et al., 2022; Neusch et al., 2022; Zhao et al., 2022a; Prelogović et al., 2022), but some key problems arise: the fine-tuning of hyperparameters and the training process is time-consuming, needs a lot of training data to optimize the learnable parameters, and may lead to sub-optimal trained models (Zhao et al., 2022a; Prelo-

gović et al., 2022).

To solve these problems, people are injecting inductive bias into CNNs with scattering transform (Mallat, 2012; Allys et al., 2019; Cheng et al., 2020; Pedersen et al., 2022) and utilize the scattering transform to construct scattering or wavelet networks (Gauthier et al., 2021; Pedersen et al., 2022). Compared with CNNs, the scattering transform uses filters having well-behaving mathematical structures like the Morlet filters (Mallat, 2012; Trott, 2016). It also uses the special design of modulus nonlinearities, and hierarchical structures, like multi-layers in a CNN, in order to extract the information across scales. With the fixed filter parameters, the scattering transform has the appeal of no need for training, which will be helpful when the training data is scarce and expensive to generate. In 3D applications, the harmonic-related wavelets (Eickenberg et al., 2017; 2018; Saydjari et al., 2021; Valogiannis & Dvorkin, 2022; Chung, 2022; Eickenberg et al., 2022) are introduced to predict molecular properties or cosmological parameters. Specifically, in Eickenberg et al. (2022), the authors use the first-order wavelet-based features and emphasize the superiority of harmonic wavelets compared with the isotropic and oriented ones. In this work, to extract information from the light cuboids (referred to as light-cones, following the trend in the literature), we utilize the solid harmonic wavelet scattering transform (Solid harmonic WST, Eickenberg et al., 2017; 2018) which injects the inductive bias into 3D CNNs with not only 3D solid harmonic wavelets but the scattering transform which outputs multiple-order wavelet-based features.

Conventional CNNs also give only the point estimate of the true parameters, not parameter posteriors, in the Bayesian view. In the case where the likelihood is intractable, the so-called implicit likelihood inference (ILI; Alsing et al., 2018; 2019; Papamakarios, 2019; Cranmer et al., 2020; Tejero-Cantero et al., 2020) (also called simulation-based inference or likelihood-free inference) is proposed to learn the density of the likelihood or posterior directly from data, with the key methodology like conditional masked autoregressive flows (CMAFs, Papamakarios et al., 2017) which is a kind of normalizing flows (Papamakarios et al., 2021). In light of this, we construct a 3D ScatterNet that combines CMAFs with Solid harmonic WST to infer the parameter posteriors from 21 cm light-cones, compare 3D ScatterNet with

---

<sup>1</sup>Department of Astronomy, Tsinghua University, Beijing, China <sup>2</sup>Institut d’Astrophysique de Paris, CNRS & Sorbonne Université, Paris, France <sup>3</sup>National Astronomical Observatories, Chinese Academy of Sciences, Beijing 100101, China <sup>4</sup>Key Laboratory of Radio Astronomy and Technology, Chinese Academy of Sciences, A20 Datun Road, Chaoyang District, Beijing, 100101, P. R. China. Correspondence to: Xiaosheng Zhao <xszhao20@gmail.com>.

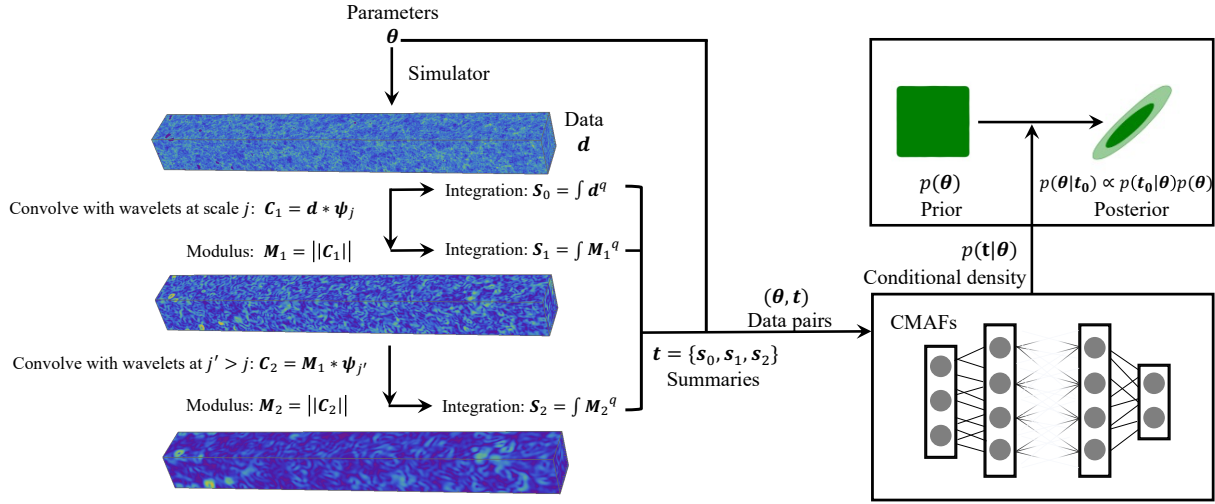


Figure 1. 3D ScatterNet. Left: Solid harmonic WST, the 3D light-cone  $\mathbf{d}$  simulated from parameter  $\theta$  are compressed by a cascade of scattering transforms, each containing convolution with wavelets, harmonic modulus (Eickenberg et al., 2017), and integration operation. The integration with raised power  $q$  gives the zeroth-, first-, and second-order coefficients  $\{S_0, S_1, S_2\}$  which form the summaries  $\mathbf{t}$ . Right: CMAFs, used to learn the summary density conditional on the parameters, with which the posterior can be inferred at  $t_0$ .

similar methods using 3D CNN in the literature, and with the conventional statistics 21 cm power spectrum for varied light-cone effects and signal contamination.

## 2. Method

The wavelet used in the Solid harmonic WST is the solid harmonic multiplying by a Gaussian and can be dilated to capture features of the field at different scales. A power  $q$  is applied to the modulus operators and results in coefficients that are sensitive to different amplitudes of fields. The covariance properties (both in translation and rotation) can be obtained by aggregating the sub-angle information represented by the angular frequency  $m$  within each  $l$ , and the invariant coefficients can be obtained by integrating over all pixels in the covariant maps. Successive group of wavelets with scales larger than the previous one can be convolved with the previous modulus, in order to get final coefficients that capture the information across scales. Apart from the aforementioned advantage of Solid harmonic WST over 3D CNNs, the ability to apply large kernels easily is also useful to recognize large HII bubbles in the 21 cm light-cones; Along the line-of-sight, the wavelets can both retain the local information and preserve some large scale information underneath the long tail of the wavelets. Part of the invariance properties (Eickenberg et al., 2017) of coefficients inherited from the harmonics-the translation invariance over sky directions and the rotation invariance over the redshift axis can benefit the following conditional density learning.

We calculate the coefficients up to an order of two including

the 0th-order coefficients which are defined as the sum of all pixel values raised by the power  $q$ . We choose the maximum angular frequency number  $L = 6$  so that  $l \in \{0..L\}$  leads to both the solid harmonic wavelets ( $l > 0$ ) which sample angular frequencies capable of decoding underlying structures like filaments, and Gaussian wavelets ( $l = 0$ ) that may characterize the ionizing process. We also choose the maximum scale  $J = 5$ , the modulus power  $q \in \{0.5, 1, 2\}$  for the first and second-order coefficients, and the (half) width parameter “sigma” being 1. For these two orders of coefficients, we average the information over different  $l$  for each  $q$ . For the zeroth-order coefficients,  $q = 0.5$  can lead to the complex number when the integration is negative and  $q = 1$  is simply zero, so we choose three higher modulus power  $q \in \{2, 3, 4\}$ . The final data summary is concatenated by these coefficients flattened over the  $q$  and  $J$  axes (except the zeroth-order coefficients which have no  $j$  dependence) and has a dimension of 66 which can be decreased by need. We follow Allys et al. (2019) and calculate the logarithms (base 2) of these coefficients before averaging (for negative components, we perform the logarithms on their absolute values while keeping their signs). In this work, the Solid harmonic WST is implemented with `Kymatio` (Andreux et al., 2018) and calculated on  $66 \times 66 \times 660$  or  $66^3$  grids depending on the light-cone dimensions.

The features extracted by the Solid harmonic WST serve as the input of CMAFs which aims to perform the implicit likelihood inference, as shown in Fig. 1. For CMAFs, we set two neural layers of a single transform, 50 neurons per layer. We also use the ensembles of CMAFs to improve the

performance, The number of transforms and the details of ensembles are chosen based on the performance of posterior validation (Zhao et al., 2022a) where the hypothesis tests are adopted to check, statistically, if the posteriors from CMAFs are self-consistent. Note that some works refer to this kind of validation as the calibration, though we do not use this method to calibrate the trained networks. Instead, we use it to indicate if the network complexity and training data are enough to learn the conditional density accurately in a statistical way. The CMAFs are implemented with `pydelfi` (Papamakarios et al., 2018; Lueckmann et al., 2019; Alsing et al., 2018; 2019) and the CMAFs architectures and training details used in this paper can be found in Appendix A.

### 3. Data

In this work, we use the publicly available code `21cmFAST` (Mesinger & Furlanetto, 2007; Mesinger et al., 2011), which can be used to perform semi-numerical simulations of reionization, as the simulator to generate our 21 cm brightness temperature datasets. Following the interpolation approach in Zhao et al. (2022a), we generate a light-cone of the size  $100 \times 100 \times 1000$  comoving  $\text{Mpc}^3$  (or  $66 \times 66 \times 660$  grid cells) in the redshift range  $7.51 \leq z \leq 11.76$ . We parametrize our reionization model as follows:  $T_{\text{vir}}$ , the minimum virial temperature of halos that host ionizing sources. We vary this parameter as  $4 \leq \log_{10}(T_{\text{vir}}/\text{K}) \leq 6$ ;  $\zeta$ , the ionizing efficiency, varied as  $1.0 \leq \log_{10}(\zeta) \leq 2.4$ . We use the logarithmic parameters for training, validation, and testing unless stated otherwise. For the signal with the first level of contamination, dubbed “pure signal”, we simply remove the mode with  $\mathbf{k}_{\perp} = 0$ , because radio interferometers cannot measure this mode. For the signal with the second level of contamination, dubbed “noised signal”, we consider 1000-hour SKA1-Low observation of the 3D 21 cm light-cones and use `Tools21cm` (Giri et al., 2020) to produce the instrumental thermal noise, where we assume 6-hour observation per day and 10 seconds of integration time. The SKA UV coverage is calculated at each frequency channel (out of 660) and used to generate the telescope response on images and suppress the thermal noise. We also smooth the images using a 1-km baseline to increase the signal-to-noise ratio. We also use `pygsm` to simulate the foregrounds based on the GSM-building model (Zheng et al., 2017), and use the singular value decomposition (SVD, Masui et al., 2013) for foreground removal, where we regard the first 6 components in the singular matrix as the foreground.

### 4. Results

**Pure signal:** For the pure signal, we use 18,000 samples for the training and validation of CMAFs. The results for two representative models are shown in Fig. 2 panel (a). We find that the results from `3D ScatterNet` have a

Table 1. Statistical quantities from 300 testing samples: the coefficient of determination  $R^2$  (calculated in logarithmic parameter space) and the 68% confidence interval of the fractional errors  $\epsilon = (y_{\text{pred}} - y_{\text{true}})/y_{\text{true}}$  (with unit  $\times 10^{-1}$ , calculated in original parameter space). Both are based on medians of the inferred posteriors and show  $T_{\text{vir}}$  and  $\zeta$  ordered in rows. {PS, ST} represent {21cmDELFI-PS, 3D ScatterNet}. 3D ScatterNet shows superiority on both quantities for both pure and noised signals.

	PURE SIGNAL		NOISED SIGNAL	
	PS	ST	PS	ST
$R^2$	0.9989	<b>0.9997</b>	0.7981	<b>0.8348</b>
	0.9978	<b>0.9990</b>	0.8028	<b>0.8254</b>
$\epsilon$	[-0.3, 0.3]	[-0.2, 0.2]	[-2.8, 4.7]	[-2.8, 4.1]
	[-0.4, 0.3]	[-0.2, 0.2]	[-2.6, 3.6]	[-2.2, 3.2]

significant improvement over that from DELFI-3DCNN which is quoted from Zhao et al. (2022a). In that work, the authors applied ILI but with data summaries with equal dimensions to the parameters compressed from a trained 3D CNN.

Note that in the reference paper, the authors used the same simulation settings as ours, but with 9000 samples for training and validation of the 3D CNN and 9000 samples for training and validation of the density estimators. As we repeat with the same experimental settings and increase the training sample size to 18,000 for both 3D CNN and density estimators, we did not get a better performance for these two fiducial models, implying that the performance is mainly limited by the hyper-parameter (including the network architecture) choice in 3D CNN. We also construct a 3D residual network (ResNet) to train a data compressor. However, our limited number of tests show worse performance than the 3D CNN used here. Further fine-tuning efforts are left to future works.

We also show the comparison with 21cmDELFI-PS which is quoted from Zhao et al. (2022b). In 21cmDELFI-PS, the authors perform ILI with the power spectrum as the summary that is a concatenated vector (with a dimension of 130) from 10 cubic light-cone boxes, where for each box, the authors choose to group the modes in Fourier space into 13 k-bins. Comparing 3D ScatterNet with 21cmDELFI-PS, the estimated  $1\sigma$  marginal errors in the former are  $1.2 - 2\times$  smaller than in the latter. In the following, we focus on the comparison of these two methods.

Next, we test the trained NDEs on 300 samples. In the second row of Table 1, we present the coefficient of determination  $R^2$  of the logarithmic parameters. A score of  $R^2$  closer to unity indicates a better overall inference performance of this parameter. We can see both methods give a high  $R^2$  value while 3D ScatterNet still outperforms 21cmDELFI-PS. In the third row of Table 1,

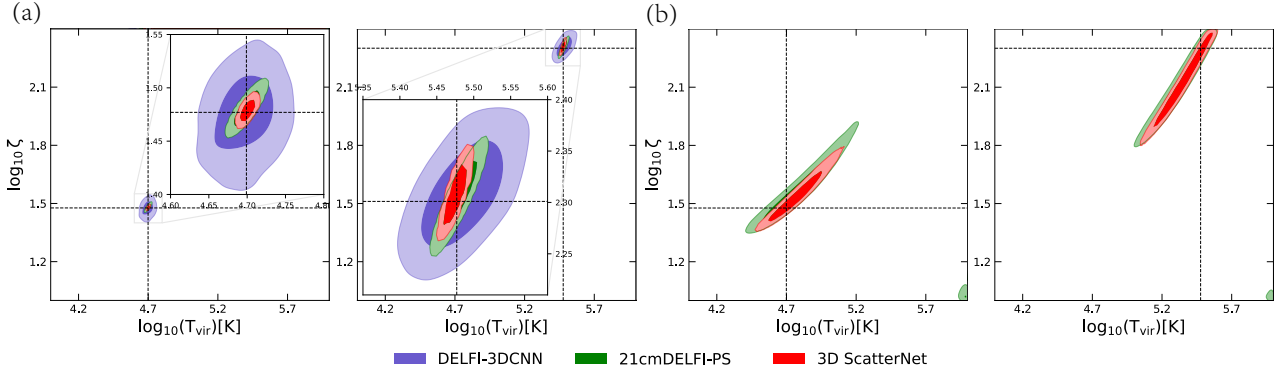


Figure 2. The posteriors inferred from the (a) pure signal and (b) noised signal, each with the same two representative models. We show the median (cross),  $1\sigma$  (dark), and  $2\sigma$  (light) confidence regions. The dashed lines indicate the true parameter values. For the pure signal, 3D ScatterNet has significant improvement over DELFI-3DCNN and has 1.2 – 2 times improvement over 21cmDELFI-PS on  $1\sigma$  marginal errors; For the noised signal, the gains of 3D ScatterNet is decreased but still non-negligible (1.2 times on average).

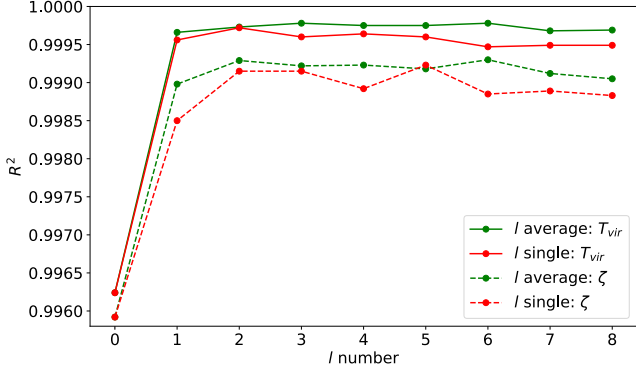


Figure 3. The  $R^2$  as a function of the angular frequency  $l$ . The “ $l$  single” uses the information of a specific  $l$  number, while the “ $l$  average” uses the average information from less than or equal to a specific  $l$  number. It is shown that solid harmonic wavelets ( $l > 0$ ) have better performance than Gaussian wavelets ( $l = 0$ ). The combination of the two has the best  $R^2$ .

we present the 68% confidence interval of the fractional errors,  $\epsilon = (y_{\text{pred}} - y_{\text{true}})/y_{\text{true}}$ , where  $y$  represents the deduced parameter (in the linear scale),  $T_{\text{vir}}$  and  $\zeta$ , and  $y_{\text{pred}}$  are medians of the inferred posteriors. The fractional errors from 3D ScatterNet have about 1.5 (1.75) times improvement in terms of the width of the 68% confidence interval) for  $T_{\text{vir}}$  ( $\zeta$ ). In Fig. 3, we show the  $R^2$  of the logarithmic parameters from another two sets of experiments. We first use the information from a single  $l$  (“ $l$  single”). The  $l = 0$ , corresponding to a Gaussian wavelet, leads to the smallest  $R^2$ . Then we use the averaged information from different  $l$  (“ $l$  average”). Compared  $l = 0$  with other points, the solid harmonic wavelet can lead to better performance than the Gaussian wavelet, and combining the two

Table 2. Similar to Table 1 but only shows the 68% confidence interval of the fractional errors  $\epsilon$  from light-cubes ( $66^3$  grids) for the pure signal. The two light-cubes correspond to the central redshifts {8.36, 9.11}. The “FULL” represents the full-band light-cones used for the main results of this paper. 3D ScatterNet (ST) also shows better performance than 21cmDELFI-PS (PS) for light-cubes with less light-cone effects.

	LIGHT-CUBE <sub>1</sub>	LIGHT-CUBE <sub>2</sub>	FULL
$\epsilon_{\text{PS}}$	[-0.6, 0.8] [-0.5, 0.8]	[-0.7, 0.8] [-0.8, 0.7]	[-0.3, 0.3] [-0.4, 0.3]
$\epsilon_{\text{ST}}$	[-0.3, 0.4] [-0.4, 0.5]	[-0.5, 0.4] [-0.6, 0.4]	[-0.1, 0.1] [-0.2, 0.2]

(by average) has the best  $R^2$ . In Table 2, we also show the results from light-cubes ( $66^3$  grids), where the light-cone effect is less obvious. We adjust the training sample size as shown in Appendix A, in order to get posteriors meeting our validation (calibration) standard. For each specific redshift, 3D ScatterNet also has better performance than 21cmDELFI-PS. A natural extension of our work is to modify the 3D ScatterNet by concatenating the scattering coefficients from discrete boxes, with the caveat that there are much more coefficients and thus it is harder to train the CMAFs.

The results above are shown to be statistically reliable with the validation methods we use. From the hypothesis tests for validation, we claim that our results are at least reliable with a significance of 0.01. We emphasize the importance of using the validation methods to ensure the CMAFs can learn self-consistent posteriors. The improvement of 3D ScatterNet over 21cmDELFI-PS implies that the Solid harmonic WST may better capture the inherent non-Gaussianity and the evolution information of the 21 cm light-cones. We visualize the coefficients from Solid har-

monic WST in Appendix B for a better understanding of how these coefficients constrain the astrophysical parameters.

**Noised signal:** For the noised signal, we use 36,000 samples for the training and validation of CMAFs. Since the images after the smoothing with a 1-km baseline lose the small-scale information, we discard the components of scattering coefficients with  $j = 0$  and the final coefficients have the dimension of 48. For the power spectrum, its dimension is reasonably reduced to 70 with little information loss. The inference results are shown in Fig. 2 panel (b), where we concatenate the MCMC chains from 10 mock observations each with a different realization of thermal noise. The results from 3D ScatterNet also have slight improvement compared with that from 21cmDELFI-PS in terms of  $1\sigma$  marginal error. From the last two columns of Table 1, the  $R^2$  from 3D ScatterNet are about 5% (3%) higher for  $\log_{10}(T_{\text{vir}})$  ( $\log_{10}\zeta$ ) and the fractional errors have about 1.09 (1.15) times improvement for  $T_{\text{vir}}$  ( $\zeta$ ).

## 5. Summary

In this work, we build a 3D ScatterNet by combining the Solid harmonic WST, a 3D CNN featurizer with inductive bias, with CMAFs in order to perform implicit likelihood inference (ILI) from 21 cm light-cones. After using the posterior validation tools to choose the CMAFs architecture and the proper size of training sets, we find that solid harmonic wavelets can enhance the performance compared with using Gaussian wavelets alone. 3D ScatterNet has significant improvement over using 3D CNN for ILI in the literature. Our results show that the Solid harmonic WST produces informative summaries more robustly and efficiently compared with a 3D CNN resulting from a reasonable amount of fine-tuning, while we note that the 3D CNN architecture adopted in this reference paper may not be optimal and could be improved by introducing further inductive bias in the networks or adopting a learnable version of 3D scattering transform. We also find improvements over using 21 cm power spectrum for ILI regarding varied light-cone effects and signal contamination, implying that applying Solid harmonic WST to full-band light-cones better captures the inherent non-Gaussianity and evolution information in line-of-sight, at either small or large scales, without splitting light-cones. Our results show that 3D ScatterNet possesses the potential for parameter inference with future 21 cm light-cones and other line intensity mappings.

## Acknowledgements

This work was supported by the National SKA Program of China (grant No. 2020SKA0110401), NSFC (grant No. 11821303), and National Key R&D Program of China

(grant No. 2018YFA0404502). We thank Yuan-Sen Ting for his kind help in preparing the initial version of the manuscript for submission. We also thank the reviewers for giving useful comments to improve this manuscript. We acknowledge the Tsinghua Astrophysics High-Performance Computing platform at Tsinghua University for providing computational and data storage resources that have contributed to the research results reported within this paper.

## References

- Allys, E., Levrier, F., Zhang, S., Colling, C., Regalado-Saint Blancard, B., Boulanger, F., Hennebelle, P., and Mallat, S. The RWST, a comprehensive statistical description of the non-Gaussian structures in the ISM. *A&A*, 629:A115, September 2019. doi: 10.1051/0004-6361/201834975.
- Alsing, J., Wandelt, B., and Feeney, S. Massive optimal data compression and density estimation for scalable, likelihood-free inference in cosmology. *MNRAS*, 477(3): 2874–2885, July 2018. doi: 10.1093/mnras/sty819.
- Alsing, J., Charnock, T., Feeney, S., and Wandelt, B. Fast likelihood-free cosmology with neural density estimators and active learning. *MNRAS*, 488(3):4440–4458, Sep 2019. doi: 10.1093/mnras/stz1960.
- Andreux, M., Angles, T., Exarchakis, G., Leonarduzzi, R., Rochette, G., Thiry, L., Zarka, J., Mallat, S., Andén, J., Belilovsky, E., Bruna, J., LOSTANLEN, V., Hirn, M. J., Oyallon, E., Zhang, S., Cella, C., and Eickenberg, M. Kymatio: Scattering Transforms in Python. *arXiv e-prints*, art. arXiv:1812.11214, December 2018.
- Cheng, S., Ting, Y.-S., Ménard, B., and Bruna, J. A new approach to observational cosmology using the scattering transform. *MNRAS*, 499(4):5902–5914, December 2020. doi: 10.1093/mnras/staa3165.
- Chung, D. T. Exploration of 3D wavelet scattering transform coefficients for line-intensity mapping measurements. *MNRAS*, 517(2):1625–1639, December 2022. doi: 10.1093/mnras/stac2662.
- Cranmer, K., Brehmer, J., and Louppe, G. The frontier of simulation-based inference. *Proceedings of the National Academy of Sciences*, 117(48):30055–30062, 2020. ISSN 0027-8424. doi: 10.1073/pnas.1912789117. URL <https://www.pnas.org/content/117/48/30055>.
- Eickenberg, M., Exarchakis, G., Hirn, M., and Mallat, S. Solid harmonic wavelet scattering: Predicting quantum molecular energy from invariant descriptors of 3d electronic densities. In *Proceedings of the 31st International Conference on Neural Information Processing Systems*,

- NIPS'17, pp. 6543–6552, Red Hook, NY, USA, 2017. Curran Associates Inc. ISBN 9781510860964.
- Eickenberg, M., Exarchakis, G., Hirn, M., Mallat, S., and Thiry, L. Solid harmonic wavelet scattering for predictions of molecule properties. *The Journal of chemical physics*, 148(24):241732, 2018.
- Eickenberg, M., Allys, E., Moradinezhad Dizgah, A., Lemos, P., Massara, E., Abidi, M., Hahn, C., Hassan, S., Regalado-Saint Blancard, B., Ho, S., Mallat, S., Andén, J., and Villaescusa-Navarro, F. Wavelet Moments for Cosmological Parameter Estimation. *arXiv e-prints*, art. arXiv:2204.07646, April 2022. doi: 10.48550/arXiv.2204.07646.
- Gauthier, S., Thérien, B., Alsène-Racicot, L., Chaudhary, M., Rish, I., Belilovsky, E., Eickenberg, M., and Wolf, G. Parametric Scattering Networks. *arXiv e-prints*, art. arXiv:2107.09539, July 2021. doi: 10.48550/arXiv.2107.09539.
- Gillet, N., Mesinger, A., Greig, B., Liu, A., and Ucci, G. Deep learning from 21-cm tomography of the cosmic dawn and reionization. *MNRAS*, 484:282–293, March 2019. doi: 10.1093/mnras/stz010.
- Giri, S. K., Mellema, G., and Jensen, H. Tools21cm: A python package to analyse the large-scale 21-cm signal from the epoch of reionization and cosmic dawn. *Journal of Open Source Software*, 5(52):2363, 2020. doi: 10.21105/joss.02363. URL <https://doi.org/10.21105/joss.02363>.
- Lueckmann, J.-M., Bassetto, G., Karaletsos, T., and Macke, J. H. Likelihood-free inference with emulator networks. In Ruiz, F., Zhang, C., Liang, D., and Bui, T. (eds.), *Proceedings of The 1st Symposium on Advances in Approximate Bayesian Inference*, volume 96 of *Proceedings of Machine Learning Research*, pp. 32, Montreal, 02 Dec 2019. PMLR.
- Mallat, S. Group invariant scattering. *Communications on Pure and Applied Mathematics*, 65(10):1331–1398, 2012. doi: <https://doi.org/10.1002/cpa.21413>. URL <https://onlinelibrary.wiley.com/doi/abs/10.1002/cpa.21413>.
- Masui, K. W., Switzer, E. R., Banavar, N., Bandura, K., Blake, C., Calin, L. M., Chang, T. C., Chen, X., Li, Y. C., Liao, Y. W., Natarajan, A., Pen, U. L., Peterson, J. B., Shaw, J. R., and Voytek, T. C. Measurement of 21 cm Brightness Fluctuations at  $z \sim 0.8$  in Cross-correlation. *ApJ*, 763(1):L20, January 2013. doi: 10.1088/2041-8205/763/1/L20.
- Mesinger, A. and Furlanetto, S. Efficient Simulations of Early Structure Formation and Reionization. *ApJ*, 669(2):663–675, November 2007. doi: 10.1086/521806.
- Mesinger, A., Furlanetto, S., and Cen, R. 21cmfast: a fast, seminumerical simulation of the high-redshift 21-cm signal. *MNRAS*, 411(2):955–972, 2011. doi: 10.1111/j.1365-2966.2010.17731.x. URL <http://dx.doi.org/10.1111/j.1365-2966.2010.17731.x>.
- Neusch, S., Heneka, C., and Brüggem, M. Inferring astrophysics and dark matter properties from 21 cm tomography using deep learning. *MNRAS*, 511(3):3446–3462, April 2022. doi: 10.1093/mnras/stac218.
- Papamakarios, G. Neural Density Estimation and Likelihood-free Inference. *arXiv e-prints*, art. arXiv:1910.13233, October 2019.
- Papamakarios, G., Pavlakou, T., and Murray, I. Masked autoregressive flow for density estimation. In *Proceedings of the 31st International Conference on Neural Information Processing Systems, NIPS'17*, pp. 2335, Red Hook, NY, USA, 2017. Curran Associates Inc. ISBN 9781510860964.
- Papamakarios, G., Sterratt, D. C., and Murray, I. Sequential Neural Likelihood: Fast Likelihood-free Inference with Autoregressive Flows. *arXiv e-prints*, art. arXiv:1805.07226, May 2018. doi: 10.48550/arXiv.1805.07226.
- Papamakarios, G., Nalisnick, E., Rezende, D. J., Mohamed, S., and Lakshminarayanan, B. Normalizing flows for probabilistic modeling and inference. *Journal of Machine Learning Research*, 22(57):1–64, 2021. URL <http://jmlr.org/papers/v22/19-1028.html>.
- Pedersen, C., Ho, S., and Eickenberg, M. Learnable wavelet neural networks for cosmological inference. In *Machine Learning for Astrophysics*, pp. 40, July 2022.
- Prelogović, D., Mesinger, A., Murray, S., Fiameni, G., and Gillet, N. Machine learning astrophysics from 21 cm lightcones: impact of network architectures and signal contamination. *MNRAS*, 509(3):3852–3867, January 2022. doi: 10.1093/mnras/stab3215.
- Saydjari, A. K., Portillo, S. K. N., Slepian, Z., Kahraman, S., Burkhart, B., and Finkbeiner, D. P. Classification of Magnetohydrodynamic Simulations Using Wavelet Scattering Transforms. *ApJ*, 910(2):122, April 2021. doi: 10.3847/1538-4357/abe46d.
- Tejero-Cantero, A., Boelts, J., Deistler, M., Lueckmann, J.-M., Durkan, C., Gonçalves, P. J., Greenberg, D. S., and Macke, J. H. sbi: A toolkit for simulation-based inference. *Journal of Open Source Software*, 5(52):2505,

2020. doi: 10.21105/joss.02505. URL <https://doi.org/10.21105/joss.02505>.

Trott, C. M. Exploring the evolution of reionization using a wavelet transform and the light cone effect. *MNRAS*, 461(1):126–135, 06 2016. ISSN 0035-8711. doi: 10.1093/mnras/stw1310. URL <https://doi.org/10.1093/mnras/stw1310>.

Valogiannis, G. and Dvorkin, C. Towards an optimal estimation of cosmological parameters with the wavelet scattering transform. *Phys. Rev. D*, 105(10):103534, May 2022. doi: 10.1103/PhysRevD.105.103534.

Zhao, X., Mao, Y., Cheng, C., and Wandelt, B. D. Simulation-based Inference of Reionization Parameters from 3D Tomographic 21 cm Light-cone Images. *ApJ*, 926(2):151, February 2022a. doi: 10.3847/1538-4357/ac457d.

Zhao, X., Mao, Y., and Wandelt, B. D. Implicit Likelihood Inference of Reionization Parameters from the 21 cm Power Spectrum. *arXiv e-prints*, art. arXiv:2203.15734, March 2022b.

Zheng, H., Tegmark, M., Dillon, J. S., Kim, D. A., Liu, A., Neben, A. R., Jonas, J., Reich, P., and Reich, W. An improved model of diffuse galactic radio emission from 10 MHz to 5 THz. *MNRAS*, 464(3):3486–3497, January 2017. doi: 10.1093/mnras/stw2525.

## A. CMAFs architectures and training details

In `pydelfi`, we set two neural layers of a single transform, 50 neurons per layer, for all CMAFs architectures. We also use the ensembles of CMAFs which are shown to be more effective compared with the single CMAF for small size of the training sample. For the training of CMAFs, we split and use 10% of the training samples for additional validation. We also use the batch size of 50, epochs of 2000, and patience of 20 for early stopping. We fine-tune the size of training sample and the CMAFs architecture for each method and each experiment, after the results of posterior validation (calibration). The general idea for the fine-tuning is that the data (summaries) containing more uncertainties may need more complex CMAFs like more transformations in a single CMAF, and the data (summaries) with a higher dimension may need a larger size of training sample because of the huge feature space. The details to produce the results in this paper are as follows:

3D ScatterNet:

- Pure signal (main results of light-cones). We use 18,000 samples and an ensemble of 8 CMAFs:  $(5, 6, 7, 8) * 2$ , where we use two CMAFs blocks each containing a CMAF with the number of transformations 5, 6, 7, and 8, respectively. Hereafter we use a similar convention for the illustration of CMAFs ensembles. We also find that the performance can be further enhanced slightly especially for 3D ScatterNet with double size of training samples.
- Pure signal (light-cones with the information of averaged  $l$ ). We use the ensembles from  $l = 1$  to  $l = 8$ :  $(5) * 4$ ,  $(6, 7, 8, 9) * 3$ ,  $(6, 7, 8, 9) * 2$ ,  $(5, 6, 7, 8) * 2$ ,  $(6, 7, 8, 9) * 3$ ,  $(5, 6, 7, 8) * 2$ ,  $(5) * 4$ ,  $(5, 6, 7, 8) * 2$ .
- Pure signal (light-cones with the information of single  $l$ ). We use the ensembles from  $l = 0$  to  $l = 8$ :  $(5) * 4$ ,  $(5) * 4$ ,  $(5, 6, 7, 8) * 2$ ,  $(5) * 4$ ,  $(5, 6, 7, 8) * 2$ ,  $(5, 6, 7, 8) * 2$ ,  $(5, 6, 7, 8) * 2$ ,  $(5, 6, 7, 8) * 2$ ,  $(5, 6, 7, 8) * 2$ ,  $(5, 6, 7, 8) * 2$ .
- Pure signal (light-cubes). We use 27,000 samples and the ensembles for the 1st, 3rd, and 5th box:  $(5, 6, 7, 8) * 3$ ,  $(5, 6, 7, 8) * 3$ ,  $(5, 6, 7, 8) * 2$ .
- Noised signal. We use 36,000 samples and the ensembles:  $(20) * 2$ .

21cmDELFI-PS:

- Pure signal (main results of light-cones). We use 18,000 samples and the ensembles  $(5) * 4$ .
- Pure signal (light-cubes). For the 1st box, we use 32,596 samples and the ensembles  $(6, 7, 8, 9) * 3$ ; for the 3rd box, we use 34,044 samples and the ensembles  $(5, 6, 7, 8) * 3$ ; and for the 5th box we use 27,000 samples and the ensembles  $(5, 6, 7, 8) * 2$ .
- Noised signal. We use 36,000 samples and the ensembles  $(20) * 3$ .

## B. The sensitively of scattering coefficients to astrophysical parameters

We show the first- and second-order scattering coefficients calculated from the light-cones (pure signal) in Fig. 4 with averaged  $l$  (up to  $l = 6$ ) and  $q = 1$ . We find that increasing  $\log_{10}(T_{\text{vir}})$  ( $\log_{10}\zeta$ ) tends to have decreasing (increasing) amplitude of the coefficients at all scales. The sensitivity of the amplitude to the varying parameters implies that these coefficients have the power to constrain the two parameters. The opposite effects on the amplitude agree with our physical intuition: perturbing a specific universe with larger ionizing efficiency has a similar ionization history to perturbing with more abundant low-mass galaxies, which also implies the direction of degeneracies in the two-parameter space. Interestingly, our initial results show that only using the zeroth-order coefficients can already give the inference performance just slightly worse than 21cmDELFI-PS on one of the representative models, while it failed sampling of the posterior with the default settings of `emcee` for the other model. Further investigation is needed based on these results.



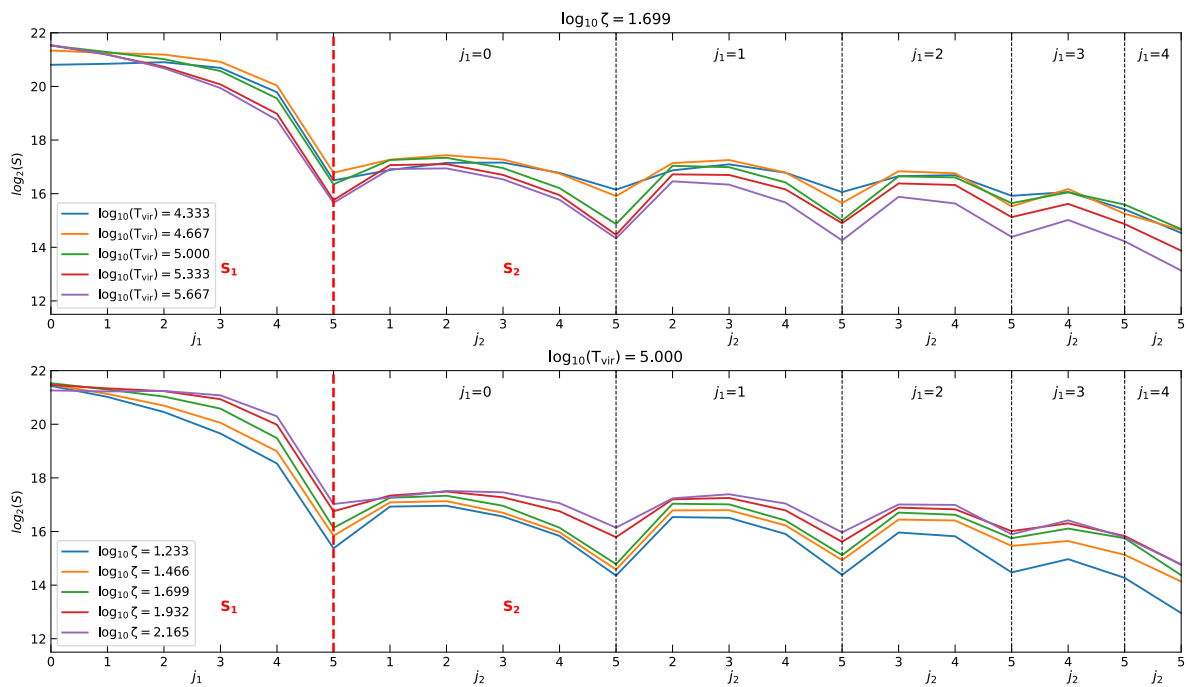


Figure 4. The first ( $S_1$ ) and second ( $S_2$ ) order solid harmonic scattering (logarithmic) coefficients with averaged  $l$  (up to  $l = 6$ ) and  $q = 1$ . We vary the two parameters  $\log_{10}(T_{\text{vir}})$  and  $\log_{10}\zeta$  in the top and bottom panel, respectively. The green lines in both the top and bottom panels are the same and are used for a clearer comparison.